

# Attosecond Optical Orientation

Lauren B Drescher,<sup>1,2,\*</sup> Nicola Mayer,<sup>3,4</sup> Kylie Gannan,<sup>1</sup> Jonah R Adelman,<sup>1</sup> and Stephen R Leone<sup>1,2,5</sup>

<sup>1</sup>*Department of Chemistry, University of California, Berkeley, California 94720, USA*

<sup>2</sup>*Chemical Sciences Division, Lawrence Berkeley National Laboratory, Berkeley, California 94720, USA*

<sup>3</sup>*Max-Born-Institut, Max-Born-Str. 2A, 12489, Berlin, Germany*

<sup>4</sup>*Attosecond Quantum Physics Laboratory, Department of Physics, King's College London, Strand, London, WC2R 2LS, United Kingdom*

<sup>5</sup>*Department of Physics, University of California, Berkeley, California 94720, USA*

(Dated: February 6, 2025)

Circularly polarized light offers opportunities to probe symmetry-dependent properties of matter such as chirality and spin. Circular dichroism measurements typically require further intrinsic or extrinsic breaking of symmetry by e.g. enantiomeric excess, orientation, magnetic fields or direction-sensitive detectors. Here we introduce circular-dichroic attosecond transient absorption spectroscopy by leveraging the angular momentum of two circular-polarized pulses, both pump and probe, in an isotropic medium, optically orienting the angular momentum of excited states on an attosecond timescale. We investigate a circular-dichroic measurement of the attosecond transient absorption of He Rydberg states. By limiting the allowed pathways via dipole selection rules for co- and counter-rotating circular polarized NIR and XUV pulses, different spectral reshaping of the XUV transient absorption due to the AC Stark effect are observed. Paired with time-dependent Schrödinger equation calculations, the results show the role of selection and propensity rules and open up new opportunities to study coupling pathways of excited states as well as spin-dependent dynamics in atoms and beyond via attosecond optical orientation.

Attosecond spectroscopy promises to follow electron dynamics in atoms, molecules and solids on their natural timescale [1]. Recent advances in the generation of circularly polarized attosecond light sources extend the opportunities to explore time-dependent dynamics that couple to the spin angular momentum of light. Most prominently, it enabled the study of time-dependent magnetization and spin dynamics in solids at the attosecond timescale under the influence of external magnetic fields [2–4]. However, many more spin and angular momentum dependent phenomena of interest exist in the absence of external magnetic fields, such as dimensional and topological [5–7], chiral [8, 9] and orientational effects [10–12].

Here, we introduce circular-dichroic attosecond transient absorption spectroscopy (cDATAS) to study  $m$  quantum number dependent coupling in isotropic media, without an external magnetic alignment field and by optical orientation [10–12] with co- and counter-rotating circularly polarized XUV+NIR two-color fields. Leveraging the selection and propensity rules in absorption and emission, we preferentially populate given excited states and show how magnetic sublevel selectivity determines the ATAS spectrum of an atom. Through the coupling of orbital and spin angular momentum, this method allows to study electron spin-dynamics [12] with attosecond time methodology. While we focus on the attosecond optical orientation in the absence of magnetic fields in this work, optical orientation previously has been used to develop sensitive atomic magnetometers [10, 11], opening the possibility to bring all-optical quantum sensing to the ultrafast domain [13]. We investigate the principle experimentally on the  $m$ -sublevel dependent coupling of the

He  $1snp$ -Rydberg series, together with time-dependent Schrödinger equation (TDSE) calculations and a perturbative model. Further applicability of the protocol is substantiated with additional experimental results on Ar and Ne autoionizing states, as well as core-exciton coupling in solid LiF. The presented study is similar in concept to ultrafast and attosecond photoionization spectroscopy studies using circular polarized, as well as co- and counter-rotating pulses in strong-field [14–17] or in multiphoton processes [18–21], however targeting the light-induced coupling between bound states and offering the excellent temporal resolution paired with the spectral resolution that transient all-optical spectroscopy methods offer.

In attosecond transient absorption, the XUV pulse induces a time-dependent dipole moment in the medium, which is modified by another pulse, such as a NIR optical pulse. The resulting emission interferes with the incoming XUV pulse, leaving fingerprints of the interaction on the XUV spectrum. In the approximation of a thin gas jet, the ATAS signal is directly related to the atomic response via [22]  $S(\omega) \propto 2\omega \text{Im} [\tilde{\mathbf{d}}(\omega) \cdot \tilde{\mathbf{E}}_{XUV}^*(\omega)]$ , where  $\tilde{\mathbf{d}}(\omega)$  and  $\tilde{\mathbf{E}}(\omega)$  are the Fourier transforms of the time-dependent dipole moment of the medium and the XUV electric field, respectively. Adding the delay-dependent NIR-field allows to prepare specific excited states, dress the medium or perturb the XUV induced dipole moment, depending on the arrival of the NIR pulse before, during or after the XUV pulse, respectively. Changing the time delay  $\tau$  between the two pulses, the underlying ultrafast dynamics can be studied with attosecond precision. In an isotropic medium like a gas jet of atoms, the accessi-

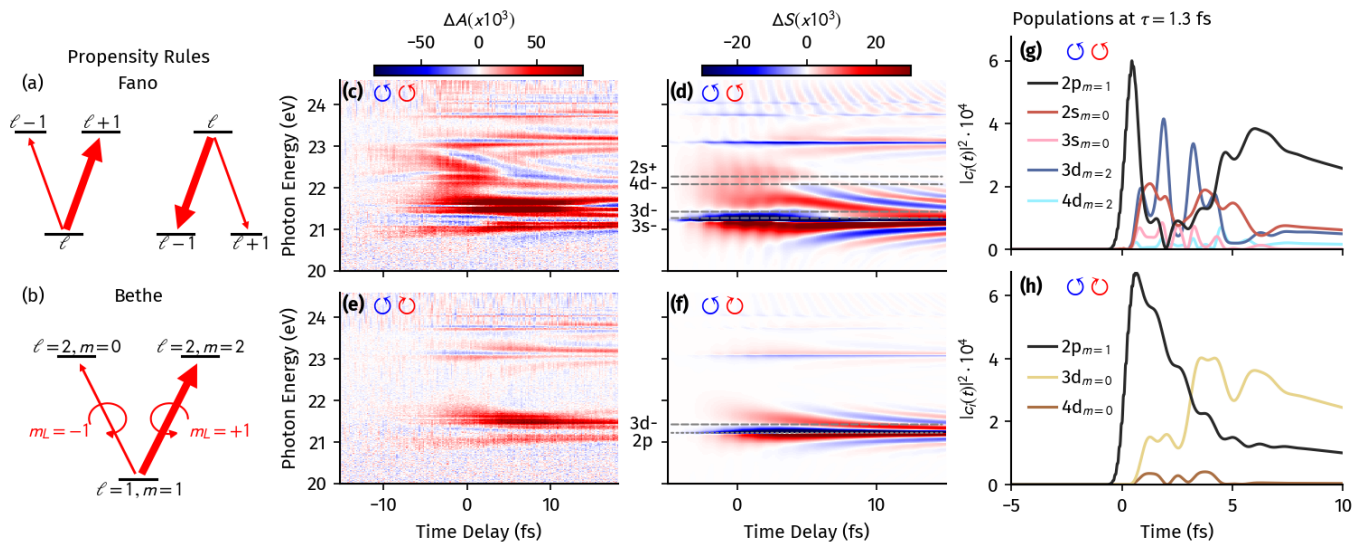


FIG. 1. Fano’s propensity rule (a) states that  $\ell$  tends to increase in absorption (left) and decrease in emission (right), as indicated by arrow size. Bethe’s propensity rule (b) indicates that  $|m|$  increases (for absorption and emission), as indicated for the transition from a  $\ell = 1, m = 1$  state. Additionally, dipole selection rules requires  $\Delta m = m_L$ , where  $m_L$  is the spin angular momentum of light. (c,e) Experimental transient absorption spectra of the He  $1snp$  Rydberg series for (c) co- and (e) counter-rotating circularly polarized XUV+NIR pulses. Similar to simulated results using TDSE (d,f), the change in absorbance shows a strong enhancement in the co- over the counter-rotating case due to the increased coupling of bright states of the  $np$  series to dark states of the  $ns$  and  $nd$  series. The light-induced states (LISs) associated with the  $2s+$ ,  $3d-$  and  $4d-$  states (around 22 eV) are strongly suppressed in the counter-rotating configuration. (g,h) Time-dependent populations of states from TDSE. The  $np_{m=1}$  states are populated by the circularly-polarized XUV pulse at 0 fs and start to decay. Population is transferred between neighboring (dark) states by the NIR pulse (centered at 1.3 fs), depending on the selection and propensity rules for the (g) co- and (h) counter-rotating NIR helicity. Only states that are populated are shown.

ble transitions are determined by the polarization of the incoming fields via the selection rules imposed on the angular momentum  $\ell$  and magnetic quantum number  $m$  of the electronic states involved. In the dipole approximation, these are  $\Delta\ell = \pm 1$  and  $\Delta m = m_L$ , where  $m_L$  is the spin angular momentum of light. The strength of a given transition is determined by its dipole matrix element  $\langle \Psi_{n\ell m} | \mathbf{d} | \Psi_{n'\ell' m'} \rangle$ , and well-known propensity rules govern the relative strength of the different transitions allowed by the selection rules. In particular, Fano’s propensity rule dictates that the absorption (emission) of photons tends to increase (decrease) the angular momentum  $\ell$  (see Fig. 1(a)) [23]. It derives from the radial part of the dipole integral  $\int_0^\infty dr \Psi_{n\ell}^*(r) r \Psi_{n'\ell'}(r)$ , or more precisely from the contribution arising from the centrifugal term  $\ell(\ell+1)/2r^2$ . Another propensity rule, stated by Bethe [24], dictates that both absorption or emission of a photon tends to increase the absolute value of the magnetic quantum number ( $|m|$ ), i.e. transition from an  $m = -1$  to  $m = -2$  sublevel is preferred over  $m = 0$ , or transition from an  $m = 2$  to an  $m = 3$  is preferred over  $m = 1$ , for the same  $\ell$  final state (see Fig. 1(b)). This rule derives from the angular part of the dipole integral, known as the Gaunt coefficient. These propensity rules arise in strong-field processes like bicircular high-harmonic generation [15] and have been observed at play in photoelec-

tron spectroscopy experiments [20, 25]. To date, they remain unstudied in ATAS experiments. Our work extends upon previous studies on the linear dichroism in attosecond transient absorption, i.e. the dependence of the dipole coupling on parallel or orthogonal polarization of XUV and NIR pulses [26] and extends the control over the angular momentum quantum number  $\ell$  in the linear dichroic case to the magnetic quantum number  $m$  in circular dichroism.

To perform these experiments, an attosecond transient absorption spectroscopy setup, previously described in more detail [4, 27], is modified to perform the circular-dichroic measurements. In brief, NIR pulses from a commercial regenerative Ti:Sa amplifier are spectrally broadened through self-phase modulation in a gas-filled stretched hollow-core fiber and compressed in time by an array of chirped mirrors and dispersive material, to a duration of less than 4 fs. The few-cycle pulse is then split in two parts at a beam splitter, with most of the pulse power being focused into a vacuum beamline into an Kr gas-flushed cell to generate XUV attosecond pulses through the process of High Harmonic Generation (HHG). The generated broadband XUV pulses are filtered from the residual driving pulse by passage through a thin Al foil and refocused by a grazing incidence toroidal mirror. Afterwards the linearly polarized

XUV beam passes through a four-mirror phase-retarder (prototype of Ultrafast Innovation Aurora). The four-fold reflection by protection-coated Mo-plates under a selectable angle leads to a phase delay between the s- and p-components of the XUV polarization and therefore produces highly elliptical polarization ( $\epsilon_{XUV} \sim \pm 0.7$ ) [28]. After passage through the polarizer, the beam focuses into the absorption cell flushed with the He target gas. The previously split-off weaker part of the few-cycle pulse travels alongside the vacuum beamline on an optical table, where a piezo-controlled delay stage allows to vary the pulse travel time to control the time-delay in the experiment. After reflection by a focusing mirror the NIR beam is co-linearly recombined with the XUV beam inside the vacuum beamline by a hole-mirror, but not before transmission through an achromatic quarter-waveplate (B. Halle RAC 4.4) mounted in a direct-drive rotation mount, allowing to rapidly modify the polarization state of the NIR pulses with varying helicity. After both beams are transmitted through the He absorption cell, a second Al foil filters the residual NIR pulse and the XUV pulse is spectrally dispersed on a flat-field grating and the spectra are imaged by a XUV-sensitized CCD camera. Additionally, a mechanical shutter in the NIR beam path allows to record XUV spectra in the presence of the NIR pulses ( $I_{\text{on}}(\omega)$ ) and with the NIR pulses blocked ( $I_{\text{off}}(\omega)$ ) in rapid succession to minimize artifacts from slow variations in the XUV spectra. This allows the delay-dependent change in absorbance  $\Delta A$  due to the pump pulse to be obtained as  $\Delta A(\omega, \tau) = -\log_{10}[I_{\text{on}}(\omega, \tau)/I_{\text{off}}(\omega)]$ .

In the experiment, the time delay between NIR and XUV pulses was varied between -15 fs to 18 fs, with 200 steps (0.166 fs steps), where the NIR pulse arrives after the XUV pulse for positive delays. A variable iris in the pump arm allows control of the NIR intensity and is set to an estimated peak intensity of  $2 \cdot 10^{12}$  W/cm<sup>2</sup>. The instrument response function (IRF) was determined to be  $5.8 \pm 0.6$  fs through NIR-induced modification of the Ne  $2s^1 2p^6 3p^1$  autoionizing resonance. To minimize artifacts due to changing beam properties, co- and counter-rotating spectra were taken in rapid succession by rotating the NIR quarter-waveplate between the  $+45^\circ$  and  $-45^\circ$  position.

The resulting transient absorption spectra for co- and counter-rotating configurations of the NIR and XUV pulses are shown in Fig. 1(c) and (e), respectively.

In the co-rotating case, the spectra show strong similarity to previous measurements on the attosecond transient absorption of He Rydberg states for co-linear polarized pulses [22, 26, 29]. Around the bright excited states of the  $1snp$  series converging towards the ionization potential at 24.59 eV, modified lineshapes are visible during and after temporal overlap of the XUV and NIR pulses due to the light-induced phase that accumulates from NIR-driven coupling to nearby dark states, as well as hy-

perbolically converging lines towards larger delays due to the truncation of the exponential decay of the time-dependent dipole moment due to NIR driven population transfer (perturbed free induction decay). In between the bright states, new resonant structures appear during overlap with the NIR pulse due to the NIR dressing of the atom, which allows for the population of one-photon dark states of the  $1sns$  and  $1snd$  series. Population is transferred to these states by additional absorption or emission of a NIR photon. Consequently, their resonance appears at plus or minus one NIR photon energy, respectively, below or above their field-free energies. We label these light-induced structures (LISs) according to their state configuration and whether their excitation followed the absorption (+) or emission (-) of a NIR photon. Such structures can be prominently found in Fig. 1(c) between the  $1s2p$  Rydberg state (21.22 eV) and  $1s3p$  Rydberg state (23.09 eV), e.g. the  $3d$ - ( $\sim 21.4$  eV),  $4d$ - ( $\sim 22.1$  eV),  $2s+$  ( $\sim 22.3$  eV) LISd, or  $3s$ - LIS ( $\sim 21.3$  eV). Due to the broad-band nature of the NIR and the decreasing spacing between Rydberg states, assignment of the individual LISs is increasingly difficult approaching the ionization potential.

The strength of many of these features appears increased compared to the case of a linearly polarized NIR pulse with the same XUV ellipticity (not shown). More strikingly, in case of a counter-rotating NIR pulse, these features appear strongly reduced if not absent as can be seen in Fig. 1(e): while the effect of the light-induced phase seems substantially reduced around the bright state resonant energies, the LISs of the  $1sns$  series are not observed and the LIS of the  $1snd$  series is heavily suppressed.

To get further physical insight into the observations, time-dependent Schrödinger equation (TDSE) calculations are employed. We use a restricted few-level model to solve the TDSE  $i\partial_t|\Psi(t)\rangle = H(t)|\Psi(t)\rangle$ , as explained in detail in Appendix B. In particular, we include the  $1sns$  series up to the  $n = 6$  state, the  $1snp$  series up to the  $n = 5$  state and the  $1snd$  series up to the  $n = 5$  state, as well as the ground state  $1s^2$ . The NIR and XUV pulse are approximated by  $\sin^2$  envelope pulses, respectively 15 fs and 1.74 fs long, with central wavelengths of  $\lambda_{NIR} = 780$  nm and  $\lambda_{XUV} = 57$  nm and intensities  $I_{NIR} = 3.51 \cdot 10^{12}$  W/cm<sup>2</sup> and  $I_{XUV} = 0.87 \cdot 10^{12}$  W/cm<sup>2</sup>. The results are shown in Fig. 1(d,f) as the single-atom response ( $\Delta S$ ), i.e. without propagation effects and scaling to the experimental absorbance ( $\Delta A$ ). The color maps show the ATAS spectrum between -5 fs and 15 fs time delay between the XUV and the NIR pulse for co-rotating (Fig. 1(d)) and counter-rotating (Fig. 1(f)) pulses, where the XUV is set to be perfectly right circularly polarized (RCP) in the calculation. It is clear that a LIS feature at  $\simeq 22.5$  eV beating at a  $2\omega_{NIR}$  frequency is observed only in the co-rotating case. Its energy matches the  $2s+$  LIS (see Fig. 1d/f). The expected position of a LIS feature

associated with the emission of one NIR photon from the  $1s4d$  state ( $4d^-$ ) is also indicated. On top of the  $2s^+/4d^-$  LISs, the LISs arising from the emission of one NIR photon from the  $1s3s$  and  $1s3d$  states also play a role, as these are almost resonant with the  $1s2p$  line (dotted line in Fig. 1(f)). In particular, the  $3d^-$  LIS splits the resonance profile when the XUV and NIR pulses overlap, reconnecting with the main  $1s2p$  line after the overlap is over at  $\tau \simeq 7.5$  fs.  $2\omega_{NIR}$  oscillations are seen from this LIS as well, as expected. Note that the  $3d^-$  LIS splits the profile of the resonance in the counter-rotating case as well, as seen in Fig. 1(f).

The time-dependent population of the excited states from TDSE calculations for the two cases are shown in Fig. 1(g,h) for a XUV+NIR time delay of  $\tau = 1.3$  fs (i.e. when the  $2s^+$  LIS is clearly present for the co-rotating case). It is clear that the NIR has the effect of shifting population off-resonantly between the  $1s2p_{m=1}$  state and the  $1s2s_{m=0}$  and  $1s3d_{m=2}$  state. The population that leaves the  $1s2p_{m=1}$  state oscillates between these two Rydberg series, with larger final population on either state depending on the relative delay between the XUV and NIR pulses, as seen also in the anti-phase beatings of their corresponding LIS features in the ATAS spectrum of Fig. 1(d). Minor population is also moved to the  $1s3s_{m=0}$  and  $1s4d_{m=2}$  states.

In the counter-rotating case, the  $m = 2$  states are no longer accessible, and population transfer occurs mainly between the  $1s2p_{m=1}$  and the  $1s3d_{m=0}$  state. Notably, no population is transferred to the  $1s2s_{m=0}$  state, as we would expect from the selection rules, since emission of a counter-rotating photon from the  $1s2p_{m=1}$  state would lead to a final spin angular momentum  $m > 0$ . Correspondingly, no LIS feature at 22.5 eV is observed in the ATAS map of Fig. 1(e,f).

Comparing the spectra obtained from TDSE calculations to the experimentally observed spectra, we note that while the general trends of co- vs counter-rotating pulses are well reproduced by the TDSE calculation, several differences are observed, especially in the specific lineshapes close to resonance. This is attributed to uncompressed satellite pulses in the NIR from higher-order dispersion as well as the relatively high gas pressure used in the experiment ( $\sim 80$  mbar), which is known to cause spectral reshaping (resonant-propagation [30]) and novel spectral structures to emerge in the vicinity of the resonances [31], as can for example be observed around the  $2p$  resonance in Fig 1(c).

Since the  $2s^+$  LIS feature is the most striking dichroic signal we observe in both experiment and theory, we focus on its circular dichroism. Fig. 2(a) shows the dichroic ATAS signal integrated around this LIS from 22 to 23 eV, where we show the normalized circular dichroism  $CD(\omega) = \frac{S_{\odot}(\omega) - S_{\ominus}(\omega)}{S_{\odot}(\omega) + S_{\ominus}(\omega)} \cdot 200\%$ , where  $S_{\odot}(\omega)$  ( $S_{\ominus}(\omega)$ ) corresponds to the ATAS signal for RCP (LCP) NIR

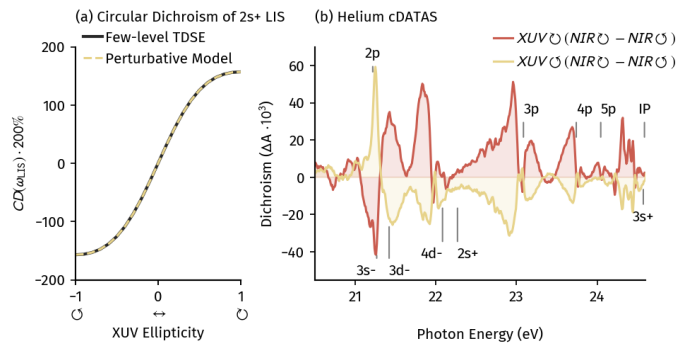


FIG. 2. (a) NIR circular dichroism signal of the  $2s^+$  LIS as a function of XUV ellipticity for the few-level TDSE calculation (black) and perturbative model (dashed yellow). (b) Experimental dichroism signal of He during temporal overlap of XUV and NIR pulses. When the XUV ellipticity is flipped from RCP  $\odot$  (blue) to LCP  $\ominus$  (red), the dichroism between RCP and LCP NIR pulses is inverted (small differences between the spectra are due to drifts in measurement conditions between experiments).

pulse. In particular, we study the CD dependence on the XUV ellipticity  $\epsilon_{XUV}$ , where  $\epsilon_{XUV} = \pm 1$  corresponds to RCP/LCP, respectively. The results are compared to a perturbative model (see Appendix C), which predicts that  $CD(\omega_{LIS}) \propto \frac{2\epsilon_X}{1+\epsilon_X^2}$ . As can be seen in Fig. 2(a), the results of the TDSE calculation follows the perturbative result closely. The circular dichroism is maximized for circularly polarized XUV and is zero for linear XUV, as one would expect. Moreover, the CD signal for opposite XUV ellipticities is reversed. This confirms that the observed dichroism originates in the different helicities of the XUV and NIR pulses: The experiments were repeated with the XUV polarizer set to the opposite helicity, which as expected reverses the role of co- and counter-rotating helicity of the NIR. Fig. 2(b) shows the circular dichroism (without normalization, averaged over the temporal overlap region,  $\tau = -2$  fs to 3 fs) for RCP ( $XUV_{\odot}$ ) and LCP XUV pulses ( $XUV_{\ominus}$ ), respectively. Due to the flip of the XUV helicity, the signal appears inverted. Small differences in the experimental signal are attributed to a drift in the measurement conditions between experiments.

Our results show that the selective excitation of  $m$  quantum number states due to the total orbital momentum coupling of circular polarized light allows to optically orient excited states in isotropic media, such as gases and centrosymmetric crystals, by investigating the spectral response of the XUV transient absorption due to co- and counter-rotating NIR pulses. The spectra thereby give insight into the electron configuration of bright excited states and their (dark state) neighbors. The method allows to explore  $\Lambda$ - versus  $V$ -type couplings, similar to four-wave-mixing [32, 33], however here due to their different selection rules of  $m$ -quantum numbers. A config-

uration that wasn't explored here additionally allows to isolate ladder-type couplings between states: A ladder-type coupling e.g.  $\ell \rightarrow (\ell + 1) \rightarrow \ell$  is not allowed for circular polarized light, while being allowed for linear polarized light. The CD behavior is not specific to this He Rydberg series but is a general result of dipole selection and propensity rules. The control over the  $m$  quantum number due to the circular-dichroism in He affects mainly the orbital angular momentum, due to the very weak spin-orbit coupling of He. However, stronger spin-orbit coupling in different systems that depart from LS-coupling will allow the XUV CD method to examine and control spin-specific excited states. Recently, we applied the cDATAS method to a series of more complex systems, in particular the Ar and Ne autoionization resonances (Fig. 3(a,b)) and solid-state LiF core-exciton resonances (Fig. 3(c)), which are discussed in more detail in Appendix A.

The results shown here are symmetric under change of helicity of the two-color field. This property arises from inversion symmetry and is not expected to hold for parity-broken systems [34], which promises novel insights for e.g. chiral molecules and non-centrosymmetric crystals [9]. While we have focused in this letter on the circular dichroism of the NIR-induced coupling in XUV-excited states, the method is also applicable to NIR- or optically-excited states. This will allow to study the evolution and spin dynamics of optically excited states without requiring an external magnetic field [12], with the extreme temporal resolution, high spectral resolution and core-level specificity of XUV transient absorption spectroscopy. One area of high interest for this method will be materials for valleytronics due to the locking of the valley-specific (pseudo-)spin [35, 36].

## ACKNOWLEDGMENTS

Investigations were supported by the U.S. Air Force Office of Scientific Research, Grant Nos FA9550-24-1-0184 and FA9550-19-1-0314. LBD acknowledges the European Union's Horizon research and innovation programme under the Marie Skłodowska-Curie grant agreement No 101066334 — SR-XTRS-2DLayMat. NM acknowledges helpful discussions with Felipe Morales. This work was funded by UK Research and Innovation (UKRI) under the UK government's Horizon Europe funding guarantee [grant number EP/Z001390/1]. JRA acknowledges the NSF GRFP under grant No DGE 2146752 and the U.S. Department of Energy, Office of Science, Basic Energy Science (BES), Materials Sciences and Engineering Division under contract DE-AC02-05CH11231 within the Fundamentals of Semiconductor Nanowires Program (KCPY23) for personnel support.

## APPENDIX A: cDATAS OF SELECTED Ar, Ne AND LiF RESONANCES

In Fig. 3(a) the circular dichroism of the autoionizing one-electron excitation of the Ar  $3s3p^6np$  series, as well as several two-electron excitation resonances in the region between 25 eV to 36 eV, are shown. A strong CD is observed for the  $3s3p^64p$  resonance. While the  $5p$  resonance carries significantly less oscillator strength, in the counter-rotating ATA its response is nearly equal to that of the  $4p$  resonance. Similarly, while the cluster of two-electron resonances of the  $3s^23p^4n'l'nl$  ( $B$  in Fig. 3(a)) type near 34 eV shows a strong CD response, the cluster between 31 eV to 32 eV ( $A$  in Fig. 3(a)) only shows a minor CD. Notably, the resonances in the  $A$  region leave the ionic core  $3s^23p^4$  in a predominantly  $^3P$  configuration, while a singlet configuration ( $^1S$  and  $^1D$ ) is more prevalent in the  $B$  region [37]. Due to the small spin-orbit splitting of the Ar lines, more insight into the non-LS type spin-orbit coupling of Ar autoionizing resonances will be gained from a detailed study of the cDATAS, complementary to recent approaches in photoelectron spectroscopy [17, 38]. In Fig. 3(b) the cDATAS of Ne between 44.5 eV to 48 eV is shown. A strong CD for the  $2s2p^63p$  autoionizing resonance is observed, while higher  $np$  resonances show only a weak response. Attosecond four-wave mixing spectroscopy recently highlighted the role of the  $3d$  dark state for the NIR induced coupling of the  $3p$  resonance [39]. Notably the  $4p$  resonance lies above the  $3d$  dark state, which would allow additional NIR coupling pathways and could explain the absence of a strong CD response. Lastly, Fig. 3(c) shows the CD of LiF core-excited states, showing the strong response of the  $X_2$  exciton arriving from a many-body excitation of the Li  $1s$ -core bands to conduction bands of predominantly Li  $2p$  character. A recent study [40] has used the linear dichroism of parallel and orthogonally polarized XUV+NIR pulses to investigate the light-induced coupling to dark excitons of predominantly Li  $2s$  character. Comparison to the CD could additionally identify the energy difference between these states due to the different dipole selection rules for emission and absorption of NIR photons.

## APPENDIX B: EFFECTIVE FEW-LEVEL MODEL

In the effective model we include only the relevant states and transitions. The TDSE  $i\partial_t|\Psi(t)\rangle = H(t)|\Psi(t)\rangle$  is solved in the length gauge by expanding the wavefunction on the basis of bound states  $|\Psi(t)\rangle = c_g(t)|1s^2\rangle + \sum_{n\ell m} c_{n\ell m}(t)|n, \ell, m\rangle$ , where  $|1s^2\rangle$  is the helium ground state and we denote the excited states by the quantum numbers of the excited electron, assuming the other one remains in the  $1s$  shell. We do not include the continuum states, since we are interested in the ATAS features below the ionization potential. The Hamiltonian

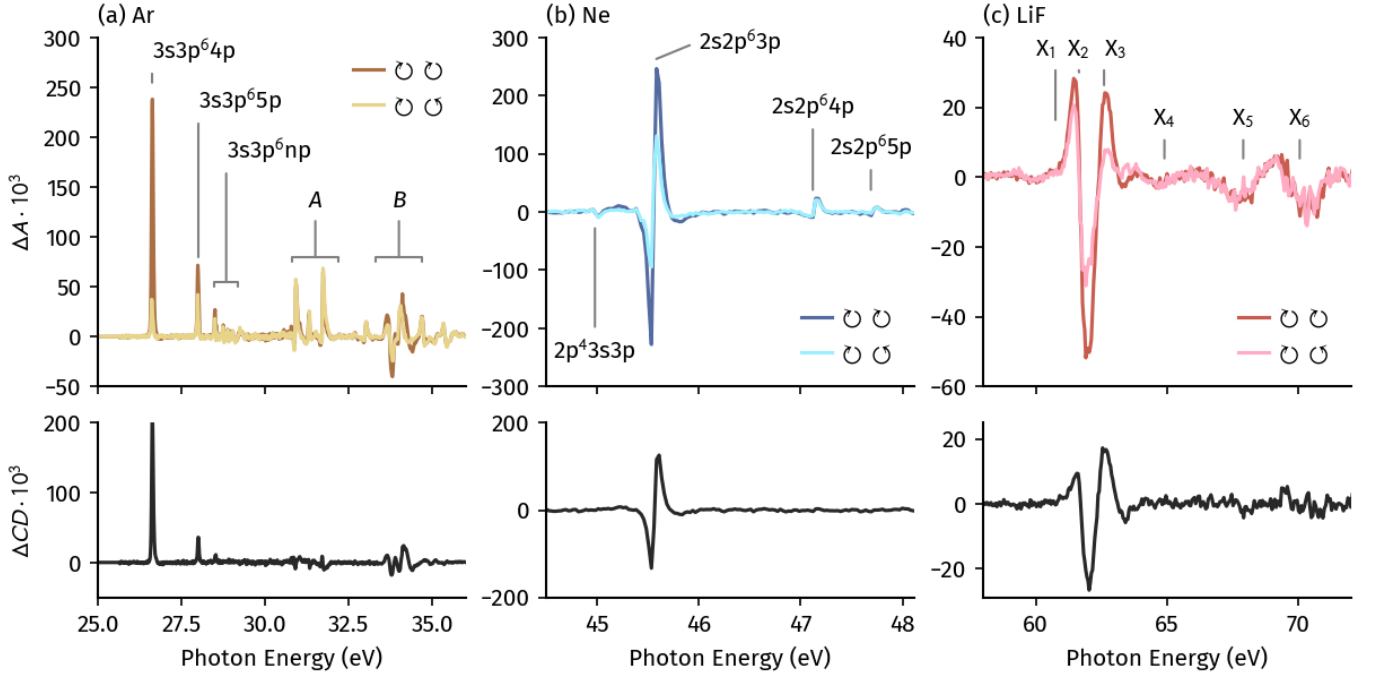


FIG. 3. (Top) Co-rotating (⊖⊖) and counter rotating (⊕⊕) and (bottom) circular dichroic XUV+NIR transient absorption spectra of selected (a) Ar, (b) Ne, and (c) LiF resonances.

$H = H_0 + V_L(t)$  consists of a field-free atomic part and the laser-matter interaction, with matrix elements given by

$$\langle i|H_0|j\rangle = E_i\delta_{ij} \quad (1)$$

$$\langle i|V_L(t)|j\rangle = -\langle i|\mathbf{d}|j\rangle \cdot \mathbf{E}(t) \quad (2)$$

where  $\mathbf{d}$  is the dipole operator,  $\mathbf{E}(t)$  is the electric field and  $E_i$  are the field-free energies of the states. The matrix elements are calculated in the quantum defect picture using field-free energies from the NIST database [16, 41, 42]. To account for the decay of the excited states we include a diagonal term in the Hamiltonian  $-i\Gamma/2$ , where  $\tau = 2/\Gamma \simeq 27$  fs. We expand the wavefunction over all magnetic quantum numbers  $m \in [-\ell, \ell]$ . The NIR and XUV fields are written in general form as

$$\mathbf{E}(t) = \frac{\mathcal{E}(t)}{\sqrt{2(1+\epsilon^2)}} \left[ \frac{1+\epsilon}{2} \mathbf{e}_+ + \frac{1-\epsilon}{2} \mathbf{e}_- \right] e^{-i\omega t} + \text{c.c.} \quad (3)$$

where  $\epsilon$  is the ellipticity,  $\mathbf{e}_+/\mathbf{e}_-$  the right-/left-circular basis, respectively, and  $\epsilon = \pm 1$  corresponds respectively to right/left-circular polarization. We assume the initial wavefunction at the start of the simulation  $t = t_0$  to be in the ground state  $|\Psi(t_0)\rangle = |1s^2\rangle$  and obtain numerically the time-dependent amplitudes  $c_i(t)$ , from which the time-dependent dipole moment  $\mathbf{d}(t) = \sum_{ij} c_i^*(t)c_j(t)\langle i|\mathbf{d}|j\rangle$  and the ATAS single-atom response  $S(\omega) = 2\omega\text{Im}[\tilde{\mathbf{d}}(\omega) \cdot \tilde{\mathbf{E}}^*(\omega)]$  can be obtained. The change in signal  $\Delta S$  is obtained by subtracting the pre-

time zero signal  $S_0$ , where the NIR field can not modify the population, from all delays. The experimental observable change in absorbance for dilute gases is proportional to the change in single-atom response through scaling with the gas density  $\rho$ :  $\Delta A \propto \frac{\rho}{\epsilon_0 c} \Delta S$ , with the vacuum permittivity  $\epsilon_0$  and the speed of light  $c$  [22].

### APPENDIX C: PERTURBATION THEORY

Here we derive the perturbative expression for the circular dichroism of the dipole moment of an atom in the presence of elliptically polarized XUV and NIR pulses, where we take the hydrogenic approximation for helium in a quantum defect picture [16, 41, 42] as in the effective few-level model. The fields are given in the helical basis as in Eq. 3. In first-order perturbation theory the absorption of an XUV photon from the ground state with  $\ell = 0$  angular momentum leads to a superposition of excited states

$$|\Psi_\epsilon(t)\rangle = c_{p_{m=1}}(t)|p_{m=1}\rangle + c_{p_{m=-1}}(t)|p_{m=-1}\rangle \quad (4)$$

where for simplicity we focus on a given state of the  $1snp$  series. In the Rotating Wave Approximation (RWA) and the short pulse limit  $\mathcal{E}_X(t) = F_X\delta(t)$ ,

$$\begin{aligned} c_{p_{m=\pm 1}}(t) &= i \frac{1 \pm \epsilon_X}{\sqrt{2(1+\epsilon_X^2)}} \int_{-\infty}^t dt' \frac{d_{s,p\pm}}{2} \mathcal{E}_X(t') e^{-i\Delta_{gp}t'} \\ &= i\Theta(t) \frac{1 \pm \epsilon_X}{\sqrt{2(1+\epsilon_X^2)}} \frac{F_X d_{s,p\pm}}{2} \end{aligned} \quad (5)$$

where  $\Theta(t)$  is the Heaviside function,  $\epsilon_X$  is the ellipticity of the XUV pulse,  $d_{s,p\pm} = \langle \Psi_g | d | np_{\pm} \rangle$  is the dipole matrix element between ground state and the  $1snp$  state with  $\ell = 1$ ,  $m = \pm 1$  and  $\Delta_{gp} = E_{np} - E_g - \omega_X$  is the detuning between the ground and  $1snp$  excited state Eigenenergies with  $\omega_X$  the central frequency of the XUV pulse. It follows that for a perfectly circularly polarized XUV pulse ( $\epsilon_X = \pm 1$ ) only either  $|p_{m=1}\rangle$  or  $|p_{m=-1}\rangle$  is populated, respectively.

Assuming a weak NIR pulse and retaining only one photon off-resonant transitions, we model its effect via a modulation by additional phases (due to the AC Stark shift) of the amplitudes. We consider the  $np$  series ( $\ell = 1$ ) coupled to the  $ns$  ( $\ell = 0$ ) and  $nd$  ( $\ell = 2$ ) ones via a one-photon transition in accordance with the selection rules  $\Delta\ell = \pm 1$ ,  $\Delta m = 0, \pm 1$ . We obtain the wavefunction:

$$|\Psi_e(t)\rangle = c_{p+1} \left( e^{i\phi_{++}(t)+i\phi_{+-}(t)} |p_{+1}\rangle + c_{p-1} \left( e^{i\phi_{-+}(t)+i\phi_{--}(t)} |p_{-1}\rangle \right) \quad (6)$$

where the phases  $\phi_{XL}$  are sorted by the helicity (+/-) of the XUV ( $X$ ) and NIR ( $L$ ) pulses, respectively:

$$\begin{aligned} \phi_{++}(t) &= \frac{(1 + \epsilon_L)^2}{2(1 + \epsilon_L^2)} \sum_n (\Delta\varphi_{p+1,nd_2} + \Delta\varphi_{p+1,ns}) \\ \phi_{+-}(t) &= \frac{(1 - \epsilon_L)^2}{2(1 + \epsilon_L^2)} \sum_n (\Delta\varphi_{p-1,nd_0} + \Delta\varphi_{p-1,ns}) \\ \phi_{-+}(t) &= \frac{(1 + \epsilon_L)^2}{2(1 + \epsilon_L^2)} \sum_n (\Delta\varphi_{p+1,nd_0} + \Delta\varphi_{p+1,ns}) \\ \phi_{--}(t) &= \frac{(1 - \epsilon_L)^2}{2(1 + \epsilon_L^2)} \sum_n (\Delta\varphi_{p-1,nd_{-2}} + \Delta\varphi_{p-1,ns}) \end{aligned} \quad (7)$$

and the light-induced phase  $\Delta\varphi$  due to the Stark shift depends explicitly on atomic parameters as [29, 43]:

$$\Delta\varphi_{p_m, n\ell_m'} = \frac{1}{2} |d_{p_m, n\ell_m'}|^2 \left( \frac{\Delta_{pn}}{\Delta_{pn}^2 - \omega_L^2} \right) \int_0^t dt' \mathcal{E}_L^2(t'), \quad (8)$$

where  $\omega_L$  is the NIR frequency,  $\mathcal{E}_L^2(t)$  the NIR intensity and  $\Delta_{pn} = E_p - E_n$ . The dipole matrix elements are given by

$$\begin{aligned} d_{p_m, n\ell_j} &= \langle p_m | r Y_{1, m-j} | n\ell_j \rangle = \\ &= \sqrt{\frac{9(2\ell+1)}{4\pi}} \begin{pmatrix} 1 & 1 & \ell \\ 0 & 0 & 0 \end{pmatrix} \begin{pmatrix} 1 & 1 & \ell \\ -m & m-j & j \end{pmatrix} \\ &\times \int_0^\infty dr R_{n1}(r) r R_{n\ell}(r), \end{aligned} \quad (9)$$

where  $R_{n1}(r)$  and  $R_{n\ell}(r)$  are the radial part of the hydrogenic wavefunctions  $\Psi_{nlm}(\mathbf{r}) = R_{nl}(r) Y_{lm}(\theta, \phi)$ , where  $R_{n1}(r)$  is the radial wavefunction of the  $p$  state with  $\ell = 1$ . Wigner's 3j-symbol for  $m_1 = m_2 = m_3 = 0$  is non-zero only if  $\ell + \ell' + \ell''$  is an even integer, and since

$$\begin{pmatrix} \ell & \ell' & \ell'' \\ m & m' & m'' \end{pmatrix} = (-1)^{\ell+\ell'+\ell''} \begin{pmatrix} \ell & \ell' & \ell'' \\ -m & -m' & -m'' \end{pmatrix} \quad (10)$$

it follows that  $S_{p+1,nd_2} = S_{p-1,nd_{-2}}$  and  $S_{p+1,ns} = S_{p-1,ns}$ . The system is therefore parity symmetric and is left unchanged by a flip of both XUV and NIR ellipticities, in contrast to a parity-breaking medium like e.g. an aligned ensemble of chiral molecules, where the flip of XUV and NIR ellipticities will lead to sizeable differences similar to the effects studied in Ref. [34].

The ATAS response is given by  $S(\omega) = \text{Im} \left[ \tilde{\mathbf{d}}(\omega) \cdot \tilde{\mathbf{E}}_{XUV}^*(\omega) \right]$ , where

$$\tilde{\mathbf{E}}_{XUV}^*(\omega) = \frac{\tilde{\mathcal{E}}^*(\omega)}{\sqrt{2(1 + \epsilon_X^2)}} \left( \frac{1 + \epsilon_X}{2} \mathbf{e}_- + \frac{1 - \epsilon_X}{2} \mathbf{e}_+ \right) + c.c. \quad (11)$$

with  $\tilde{\mathcal{E}}(\omega) = \int dt \mathcal{E}(t) \exp(i(\omega - \omega_X)t)$  and similar  $\tilde{\mathbf{d}}(\omega)$  is obtained through Fourier transformation from the time-dependent dipole moment  $\mathbf{d}(t) = \langle \Psi(t) | \mathbf{d} | \Psi(t) \rangle = \langle \Psi_g | \mathbf{d} | \Psi_e(t) \rangle + c.c.$ . The ATAS dichroism is obtained by subtracting the signal with RCP NIR from the LCP NIR one, where the XUV ellipticity is fixed

$$\text{CD}(\omega) = \text{Im} \left[ (\tilde{\mathbf{d}}_{RCP}(\omega) - \tilde{\mathbf{d}}_{LCP}(\omega)) \cdot \tilde{\mathbf{E}}_{XUV}^*(\omega) \right] \quad (12)$$

The time-dependent dipole moment for each NIR helicity is given by summation over the RCP/LCP ( $\alpha = \pm$ ) contributions:

$$\begin{aligned} \mathbf{d}_{RCP}(t) &= \frac{i\Theta(t)F_X}{2\sqrt{2(1 + \epsilon_X^2)}} \sum_{\alpha=\pm} |d_{s,p\alpha}|^2 \\ &\times (1 + \alpha\epsilon_X) e^{i\phi_{\alpha+}(t)} \mathbf{e}_\alpha + c.c. \end{aligned} \quad (13)$$

$$\begin{aligned} \mathbf{d}_{LCP}(t) &= \frac{i\Theta(t)F_X}{2\sqrt{2(1 + \epsilon_X^2)}} \sum_{\alpha=\pm} |d_{s,p\alpha}|^2 \\ &\times (1 + \alpha\epsilon_X) e^{i\phi_{\alpha-}(t)} \mathbf{e}_\alpha + c.c. \end{aligned} \quad (14)$$

and  $\Delta\mathbf{d}(t) = \mathbf{d}_{RCP}(t) - \mathbf{d}_{LCP}(t)$  is given by

$$\begin{aligned} \Delta\mathbf{d}(t) &= \frac{i\Theta(t)F_X}{2\sqrt{2(1 + \epsilon_X^2)}} \\ &\sum_{\alpha=\pm} |d_{s,p\alpha}|^2 (1 + \alpha\epsilon_X) \\ &\times \left( e^{i\phi_{\alpha+}(t)} - e^{i\phi_{\alpha-}(t)} \right) \mathbf{e}_\alpha + c.c. \end{aligned} \quad (15)$$

By transforming to frequency domain by Fourier transformation, denoting that  $d_{s,p+1} = d_{s,p-1} = d_{s,p}$  and introducing  $A_\alpha(\omega) = \int_0^\infty (e^{i\phi_{\alpha+}(t)} - e^{i\phi_{\alpha-}(t)}) e^{i\omega t}$ , using  $A_+(\omega) = -A_-(\omega)$ ,  $\mathbf{e}_+ \cdot \mathbf{e}_- = 1$  and the definition of  $\tilde{\mathbf{E}}_{XUV}^*(\omega)$  from above, the circular dichroism is given by

$$\text{CD}(\omega) = 2|d_{s,p}|^2 \frac{\epsilon_X}{1 + \epsilon_X^2} \text{Re} \left[ A(\omega) \tilde{\mathcal{E}}^*(\omega) \right]. \quad (16)$$

We see that for a linearly polarized XUV pulse along the x-axis  $\epsilon_X = 0$ , the circular dichroism is zero because the dichroic dipole moment  $\Delta\mathbf{d}(t)$  is oriented along

the y-axis. For opposite XUV ellipticities,  $CD_{\epsilon_X}(\omega) = -CD_{-\epsilon_X}(\omega)$ , as expected from parity. For parity-broken systems  $CD_{\epsilon_X}(\omega) \neq CD_{-\epsilon_X}(\omega)$ .

---

\* drescher@mbi-berlin.de; Present Address: Max-Born-Institut, Max-Born-Str. 2A, 12489, Berlin, Germany

- [1] S. R. Leone, C. W. McCurdy, J. Burgdörfer, L. S. Cederbaum, Z. Chang, N. Dudovich, J. Feist, C. H. Greene, M. Ivanov, R. Kienberger, U. Keller, M. F. Kling, Z.-H. Loh, T. Pfeifer, A. N. Pfeiffer, R. Santra, K. Schafer, A. Stolow, U. Thumm, and M. J. J. Vrakking, *Nature Photonics* **8**, 162 (2014).
- [2] F. Willems, C. T. L. Smeenk, N. Zhavoronkov, O. Kornilov, I. Radu, M. Schmidbauer, M. Hanke, C. von Korff Schmising, M. J. J. Vrakking, and S. Eisebitt, *Physical Review B* **92**, 220405 (2015).
- [3] F. Siegrist, J. A. Gessner, M. Ossiander, C. Denker, Y.-P. Chang, M. C. Schröder, A. Guggenmos, Y. Cui, J. Walowski, U. Martens, J. K. Dewhurst, U. Kleineberg, M. Münzenberg, S. Sharma, and M. Schultze, *Nature* **571**, 240 (2019).
- [4] R. Généaux, H.-T. Chang, A. Guggenmos, R. Delaunay, F. Légaré, K. Légaré, J. Lüning, T. Parpiiev, I. J. P. Molesky, B. R. de Roulet, M. W. Zuerch, S. Sharma, M. Schultze, and S. R. Leone, *Physical Review Letters* **133**, 106902 (2024).
- [5] M. Z. Hasan and C. L. Kane, *Reviews of Modern Physics* **82**, 3045 (2010).
- [6] J. R. Schaibley, H. Yu, G. Clark, P. Rivera, J. S. Ross, K. L. Seyler, W. Yao, and X. Xu, *Nature Reviews Materials* **1**, 1 (2016).
- [7] C. Bao, P. Tang, D. Sun, and S. Zhou, *Nature Reviews Physics* , 1 (2021).
- [8] S.-H. Yang, R. Naaman, Y. Paltiel, and S. S. P. Parkin, *Nature Reviews Physics* **3**, 328 (2021).
- [9] J. R. Rouxel and S. Mukamel, *Chemical Reviews* **122**, 16802 (2022).
- [10] W. Franzen and A. G. Emslie, *Physical Review* **108**, 1453 (1957).
- [11] G. V. Skrotskii and T. G. Izyumova, *Soviet Physics Uspekhi* **4**, 177 (1961).
- [12] F. Meier and B.P. Zakharchenya, *Optical Orientation, Modern Problems in Condensed Matter Sciences* (Elsevier, Burlington, MA, 1984).
- [13] E. Sutcliffe, N. P. Kazmierczak, and R. G. Hadt, *Science* **386**, 888 (2024).
- [14] A. Hartung, F. Morales, M. Kunitski, K. Henrichs, A. Laucke, M. Richter, T. Jahnke, A. Kalinin, M. Schöffler, L. P. H. Schmidt, M. Ivanov, O. Smirnova, and R. Dörner, *Nature Photonics* **10**, 526 (2016).
- [15] Á. Jiménez-Galán, N. Zhavoronkov, D. Ayuso, F. Morales, S. Patchkovskii, M. Schloz, E. Pisanty, O. Smirnova, and M. Ivanov, *Physical Review A* **97**, 023409 (2018).
- [16] N. Mayer, S. Beaulieu, Á. Jiménez-Galán, S. Patchkovskii, O. Kornilov, D. Descamps, S. Petit, O. Smirnova, Y. Mairesse, and M. Y. Ivanov, *Physical Review Letters* **129**, 173202 (2022).
- [17] S. Carlström, R. Tahouri, A. Papoulia, J. M. Dahlström, M. Y. Ivanov, O. Smirnova, and S. Patchkovskii, *Spin-Polarized Photoelectrons in the Vicinity of Spectral Features* (2024), arXiv:2306.15665 [physics].
- [18] S. Eckart, M. Kunitski, M. Richter, A. Hartung, J. Rist, F. Trinter, K. Fehre, N. Schlott, K. Henrichs, L. P. H. Schmidt, T. Jahnke, M. Schöffler, K. Liu, I. Barth, J. Kaushal, F. Morales, M. Ivanov, O. Smirnova, and R. Dörner, *Nature Physics* **14**, 701 (2018).
- [19] A. H. N. C. De Silva, T. Moon, K. L. Romans, B. P. Acharya, S. Dubey, K. Foster, O. Russ, C. Rischbieter, N. Douguet, K. Bartschat, and D. Fischer, *Physical Review A* **103**, 053125 (2021).
- [20] M. Han, J.-B. Ji, T. Balčiūnas, K. Ueda, and H. J. Wörner, *Nature Physics* **19**, 230 (2023).
- [21] A. S. Kheifets, *Physical Review Research* **6**, L012002 (2024).
- [22] M. Wu, S. Chen, S. Camp, K. J. Schafer, and M. B. Gaarde, *Journal of Physics B: Atomic, Molecular and Optical Physics* **49**, 062003 (2016).
- [23] U. Fano, *Physical Review A* **32**, 617 (1985).
- [24] H. A. Bethe and R. W. Jackiw, *Intermediate quantum mechanics, Third Edition* (CRC Press, 1997) Chap. Chapter 11.
- [25] D. Busto, J. Vinbladh, S. Zhong, M. Isinger, S. Nandi, S. Maclot, P. Johnsson, M. Gisselbrecht, A. L’Huillier, E. Lindroth, and J. M. Dahlström, *Physical Review Letters* **123**, 133201 (2019).
- [26] M. Reduzzi, J. Hummert, A. Dubrouil, F. Calegari, M. Nisoli, F. Frassetto, L. Poletto, S. Chen, M. Wu, M. B. Gaarde, K. Schafer, and G. Sansone, *Physical Review A* **92**, 033408 (2015).
- [27] B. R. De Roulet, L. Drescher, S. A. Sato, and S. R. Leone, *Physical Review B* **110**, 174301 (2024).
- [28] C. von Korff Schmising, D. Weder, T. Noll, B. Pfau, M. Hennecke, C. Strüber, I. Radu, M. Schneider, S. Staeck, C. M. Günther, J. Lüning, A. el dine Merhe, J. Buck, G. Hartmann, J. Viefhaus, R. Treusch, and S. Eisebitt, *Review of Scientific Instruments* **88**, 053903 (2017).
- [29] M. Chini, B. Zhao, H. Wang, Y. Cheng, S. Hu, and Z. Chang, *Phys. Rev. Lett.* **109**, 073601 (2012).
- [30] C.-T. Liao, A. Sandhu, S. Camp, K. J. Schafer, and M. B. Gaarde, *Physical Review Letters* **114**, 143002 (2015).
- [31] A. N. Pfeiffer, M. J. Bell, A. R. Beck, H. Mashiko, D. M. Neumark, and S. R. Leone, *Physical Review A* **88**, 051402 (2013).
- [32] J. D. Gaynor, A. P. Fidler, Y.-C. Lin, H.-T. Chang, M. Zuerch, D. M. Neumark, and S. R. Leone, *Physical Review B* **103**, 245140 (2021).
- [33] J. D. Gaynor, A. P. Fidler, Y. Kobayashi, Y.-C. Lin, C. L. Keenan, D. M. Neumark, and S. R. Leone, *Physical Review A* **107**, 023526 (2023).
- [34] L. Drescher, M. J. J. Vrakking, and J. Mikosch, *Journal of Physics B: Atomic, Molecular and Optical Physics* **53**, 164005 (2020).
- [35] A. Geondzhian, A. Rubio, and M. Altarelli, *Physical Review B* **106**, 115433 (2022).
- [36] M. Malakhov, G. Cistaro, F. Martín, and A. Picón, *Communications Physics* **7**, 1 (2024).
- [37] R. P. Madden, D. L. Ederer, and K. Codling, *Physical Review* **177**, 136 (1969).
- [38] M. Turconi, L. Barreau, D. Busto, M. Isinger, C. Alexandridi, A. Harth, R. J. Squibb, D. Kroon, C. L. Arnold, R. Feifel, M. Gisselbrecht, L. Argenti, F. Martín, A. L’Huillier, and P. Salières, *Journal of Physics B:*

- Atomic, Molecular and Optical Physics **53**, 184003 (2020).
- [39] N. G. Puskar, Y.-C. Lin, J. D. Gaynor, M. C. Schuchter, S. Chattopadhyay, C. Marante, A. P. Fidler, C. L. Keenan, L. Argenti, D. M. Neumark, and S. R. Leone, *Physical Review A* **107**, 033117 (2023).
- [40] K. J. Gannan, L. B. Drescher, R. Quintero-Bermudez, N. Rana, C. Huang, K. Schafer, M. B. Gaarde, and S. R. Leone, Polarization-Resolved Core Exciton Dynamics in LiF Using Attosecond Transient Absorption Spectroscopy (2025), arXiv:2501.18083 [cond-mat].
- [41] L. P. Yatsenko, T. Halfmann, B. W. Shore, and K. Bergmann, *Physical Review A* **59**, 2926 (1999).
- [42] A. Kramida, Yu. Ralchenko, J. Reader, and NIST ASD Team, NIST Atomic Spectra Database (ver. 5.11), [Online]. Available: <https://physics.nist.gov/asd> [2017, April 9]. National Institute of Standards and Technology, Gaithersburg, MD. (2023).
- [43] N. B. Delone and V. P. Krainov, *Physics-Uspekhi* **42**, 669 (1999).